Characterization of tracked radiofrequency ablation in phantom

Chun-Cheng R. Chen,[a] Michael I. Miga, and Robert L. Galloway
Department of Biomedical Engineering, Vanderbilt University, 5824 Stevenson Center, Nashville, Tennessee 37235

In radiofrequency ablation (RFA), successful therapy requires accurate, image-guided placement of the ablation device in a location selected by a predictive treatment plan. Current planning methods rely on geometric models of ablations that are not sensitive to underlying physical processes in RFA. Implementing plans based on computational models of RFA with image-guided techniques, however, has not been well characterized. To study the use of computational models of RFA in planning needle placement, this work compared ablations performed with an optically tracked RFA device with corresponding models of the ablations. The calibration of the tracked device allowed the positions of distal features of the device, particularly the tips of the needle electrodes, to be determined to within 1.4 ± 0.6 mm of uncertainty. Ablations were then performed using the tracked device in a phantom system based on an agarose-albumin mixture. Images of the sliced phantom obtained from the ablation experiments were then compared with the predictions of a bioheat transfer model of RFA, which used the positional data of the tracked device obtained during ablation. The model was demonstrated to predict 90% of imaged pixels classified as being ablated. The discrepancies between model predictions and observations were analyzed and attributed to needle tracking inaccuracy as well as to uncertainties in model parameters. The results suggest the feasibility of using finite element modeling to plan ablations with predictable outcomes when implemented using tracked RFA. © *2007 American Association of Physicists in Medicine*. [DOI: 10.1118/1.2761978]

I. INTRODUCTION

Radiofrequency ablation (RFA) is currently a widely used treatment modality for unresectable hepatic tumors.[1] RFA produces focal therapy by delivering electrical energy via needle electrodes directly into a cancerous lesion, resulting in thermal destruction of the tissue. Because active heating is limited spatially to within a few millimeters of the RFA needle,[2] the therapeutic efficacy of RFA depends on proper placement of the needle so that the final ablation extents would cover the tumor along with a suitable margin. At present, needle placement is performed using intraoperative image guidance, typically with two-dimensional (2D) ultrasound.[3] It has been recognized, however, that guidance with 2D ultrasound can be inaccurate.[4,5] Investigators have described various strategies of improving needle localization intraoperatively including the use of optically based and electromagnetic[6] tracking systems to determine the location of the device relative to the targeted lesion. The use of various intraoperative imaging methods to aid guidance has also been reported for CT[7] and 3D ultrasound.[8]

Although guidance provides a means of delivering the needle device to an intended destination, it depends on having a preplanned needle placement that achieves the desired therapeutic goal. Thus, successful therapy requires planning with a predictive model of RF ablations. Presently, geometric shapes using spheres and ellipses have been employed to model ablations.[9] Geometric models provide a method for rapid planning of optimal trajectories, subject to the con-straints placed by the anatomy of the patient.[10] Nevertheless, geometric shapes are not sensitive to the actual physical parameters that govern ablations. More sophisticated finite element models have been developed that attempt to solve partial differential equations describing thermal ablations.[11,12] Though there is some work describing the use of computational models of ablation with respect to preoperative planning,[13–15] there has been little effort to study their application in conjunction with guidance technology in order to direct intraoperative therapy.

This article will examine the problem of coupling positional information about a tracked RFA device with a computational model that predicts therapeutic outcome using physical principles governing RFA. The goal is to characterize the spatial extents of actual ablations performed with tracked RFA in comparison to model predictions using the positional data from the tracking. To achieve this goal, several pieces of technology, which until now investigators have studied independently, will be integrated together. First a tracked RFA device will be constructed and characterized for use in locating the functional components of the device within the coordinate frame of the treatment region. Then a phantom system will be developed to help visualize the ablation outcomes performed using the tracked RFA needle. Finally, the phantom system will be imaged, and the ablation extents will be compared with finite element models of RFA solved using the measured needle positions as inputs.
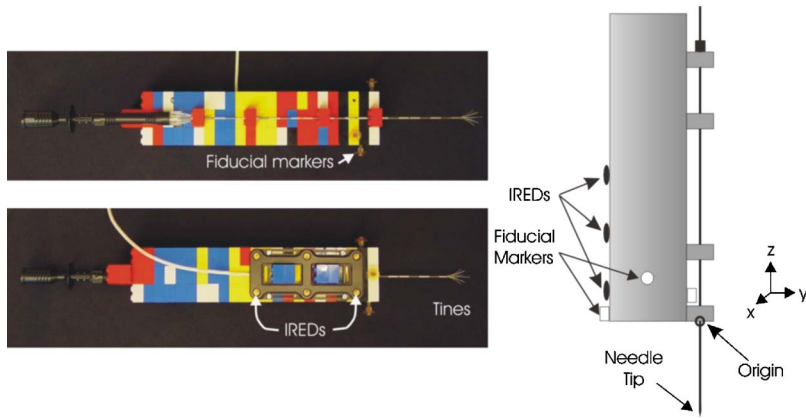
FIG. 1. Images showing the needle holder with the RFA device (top) on one side and, on the other, the IREDs (bottom) that provide position data to the Optotrak tracking system. Fiducial markers were used to coregister the CT model of the device.

II. MATERIALS AND METHODS

II.A. Tracked RFA

II.A.1. Needle holder design

The ablation device used in this study was a RITA Starburst XL model radiofrequency ablation probe (RITA Medical Systems, CA). In order to track the device in space, a rigid needle holder was constructed. The needle holder served two primary functions. First, the holder reduced the bending of the RFA needle shaft so that during placement the needle shaft could be assumed to lie on a straight line, thus facilitating guidance. Second, the holder provided a surface on which to attach infrared emitting diodes (IREDs) rigidly at places close to the distal tip of the device, where the active electrodes are deployed. By localizing IREDS in space using an optical tracking system (Optotrak 3020, Northern Digital, Inc., Waterloo, Ontario), real-time information about the location of the needle holder, and thus the needle itself, was determined.

II.A.2. Needle holder calibration

The calibration of the needle's physical location relative to the IREDs on the needle holder was achieved in two steps. The first step was to establish a local coordinate system in which the origin was placed where the needle emerged from the base of the holder (see Fig. 1). This step entailed using proprietary software (NDI Architect, Northern Digital, Inc., Waterloo, Ontario) to determine a consistent rigid body description of the IREDs. The z axis was set to run parallel to the needle shaft, and the other two axes were arbitrarily chosen. To localize the origin, the point of intersection between the needle axis and the base of the shaft was calculated. The second step of the calibration required determining the length of the shaft of the needle from the base of the holder to the needle tip. Given this length, the needle tip was tracked by offsetting the origin along the calculated needle axis. The total transformation from the needle tip in the coordinate system of the needle to the coordinate system of the holder is designated, $\mathcal{T}_{\text{needle}\rightarrow\text{holder}}$. Because this transformation is rigid, its operation on any point $\mathbf{x}$ can be written as

$$\mathcal{T}(\mathbf{x}) = \mathbf{Rx} + \mathbf{t}, \tag{1}$$

where $\mathbf{R}$ is a rotation matrix, and $\mathbf{t}$ is a translation vector.

Since the RFA device contains functional features that are not rotationally symmetric about its axis, particularly the peripheral tines that do not lie directly on the needle axis, an additional step was taken to determine the spatial relationship of the RFA tines to the needle holder. A CT image of the device was acquired while attached to the needle holder, with the tines deployed at the manufacturer's 2 cm setting (see Fig. 2). The locations of the nine tine tips on the device were manually segmented, and their positions in the image were recorded for coregistration with the needle geometry used in the computational model discussed below. Four Acustar fiducial markers[16] attached to the needle holder (see Fig. 1) were also segmented, and their centroids were coregistered with Optotrak measurements of the corresponding points. The coregistration step provided a means of mapping objects in the reference coordinates defined by the Acustar markers, most importantly the tines of the RFA device, to the reference coordinates of Optotrak. Thus this step generated $\mathcal{T}_{\text{needle}\rightarrow\text{holder}}$ specifically for the RFA device. It should be pointed out that whereas in the needle calibration, the remaining axes aside from the needle axis were arbitrarily defined due to the rotational symmetry of the needle, the coregistration of the Acustar markers in CT image and physical space produced a unique transformation.

II.A.3. Needle tracking experiment

To characterize the ability of the needle holder apparatus to track the tip of a needle, experiments were performed using a 10 in. hollow bore, 16 gauge needle (Popper and Sons, NY) as a proxy for the RFA device. The needle was attached to the tracked needle holder and inserted into various locations within a rigid polyvinyl chloride (PVC) box. On the surface of the box were placed four Acustar fiducial markers (see Fig. 3). The box was filled with a 3% w/v gelatin solution (275 Bloom, Type A, Vyse Gelatin Co., IL) to provide a solid medium into which the needle is inserted. With each needle placement, the position of the needle holder as measured by Optotrak was recorded, and then about 1 mL of a 60% w/v barium sulfate suspension (Lafay-
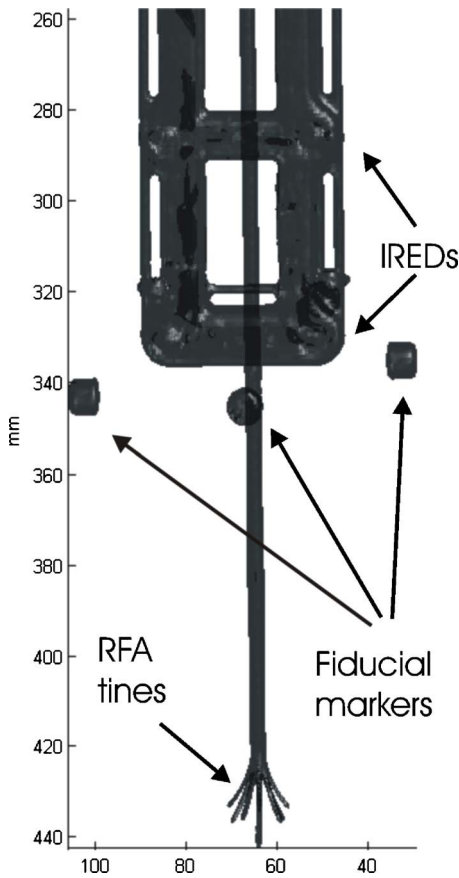
FIG. 2. Rendering of segmented CT image of RFA device attached to the needle holder showing the deployed tines. The floating objects are the Acustar markers, while the H-shaped object near the top of the image is the frame that houses the IREDs.

ette Pharmaceuticals, IN) was injected into the gelatin. The barium provided a record of where the needle was placed in the box when imaged by CT. All CT imaging for this and other experiments was conducted on a Philips Mx8000 IDT 16-slice system. Images were acquired with 1 mm slice thickness and variable pixel resolutions ranging from
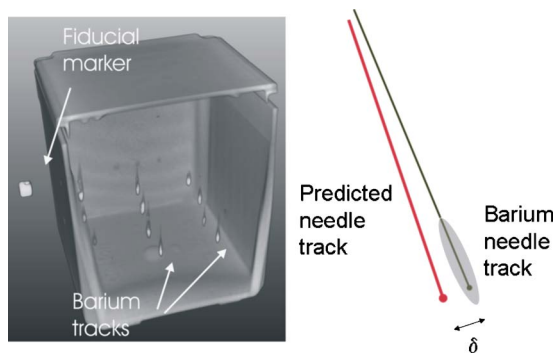

FIG. 3. (left) 3D rendering of barium tracks imaged in CT. An Acustar marker is shown on the left. (right) Schematic showing between needle tip location predicted by Optotrak measurements and the needle track segmented in the CT image.

0.4–0.5 mm. A total of 86 needle placements were recorded. The average distance from the needle tip to the origin of the needle holder was 9 cm.

In order to locate the needle tip within the CT image of the gelatin, a series of rigid body transformations was computed to convert measurements in Optotrak coordinate system to the local coordinate system of the PVC box:

$$\mathcal{T}_{\text{needle}\rightarrow\text{phantom}} = \mathcal{T}_{\text{needle}\rightarrow\text{holder}} \circ \mathcal{T}_{\text{holder}\rightarrow\text{opto}} \circ \mathcal{T}_{\text{opto}\rightarrow\text{phantom}}.$$

$$(2)$$

The transformation $\mathcal{T}_{\text{needle}\rightarrow\text{holder}}$, which mapped the tracked tip to the holder, was determined in the previous section on needle holder calibration; $\mathcal{T}_{\text{holder}\rightarrow\text{opto}}$, which gave the coordinates of the holder in the global coordinate system, was reported by the Optotrak system after each needle insertion into the gelatin phantom; and $\mathcal{T}_{\text{opto}\rightarrow\text{phantom}}$ was constructed by coregistering the physical locations of the Acustar markers with their centroids in CT segmentations.

Segmenting the barium tracks proceeded with the following thresholding scheme. For each barium track, pixel values greater than 1300 Hounsfield units were identified. Using the Optotrak measurement as a guide, the search was constrained to a trajectory-aligned cylindrical neighborhood around the needle tip location. The cylinder was set to be 3 mm in diameter in which the axis of the cylinder is aligned with the measured axis of the needle. All other pixels outside of this cylinder were discarded. The needle trajectory was then corrected by pivoting about the measured origin of the needle holder until the average weighted distance from each pixel to the trajectory was minimized. The distance was weighted by the pixel intensities so that the trajectory would preferentially fit the higher intensity pixels produced by the concentrated barium suspension. Finally, a tip location was selected by searching the most distal pixel within a 1 mm diameter of the trajectory. To quantify the discrepancy between the predicted needle tip location, $\mathbf{x}_{\text{phantom}}$, as derived using the Optotrak tracking measurements, and the observed needle tip location, $\mathbf{x}_{\text{CT}}$, as segmented in CT space, the following Euclidean distance metric is used: $\delta = |\mathbf{x}_{\text{phantom}} - \mathbf{x}_{\text{CT}}|$.

II.B. Phantom experiments

II.B.1. Ablations

The ablations were performed in a rectangular acrylic box (4 in. × 3 in. × 4.5 in.) designed with needle holes on the top surface (see Fig. 4). The needle holes were placed along the midline of the box. These holes served both as physical markers to collocalize with the model in subsequent analysis and as needle guides for controlled placement. This coregistration produced a transformation that mapped the coordinates from the Optotrak to the local coordinates of the phantom, $\mathcal{T}_{\text{opto}\rightarrow\text{phantom}}$, as previously described for the needle tracking experiment.

The box was filled with approximately 600 ml of a tissue-mimicking agarose-albumin gel adapted from Ref. 17. The gel was composed of agarose (1% w/v) mixed in with liquid egg white (Country Creek Farms, AR). According to the manufacturer, a 450 mL product contained roughly 50 g of
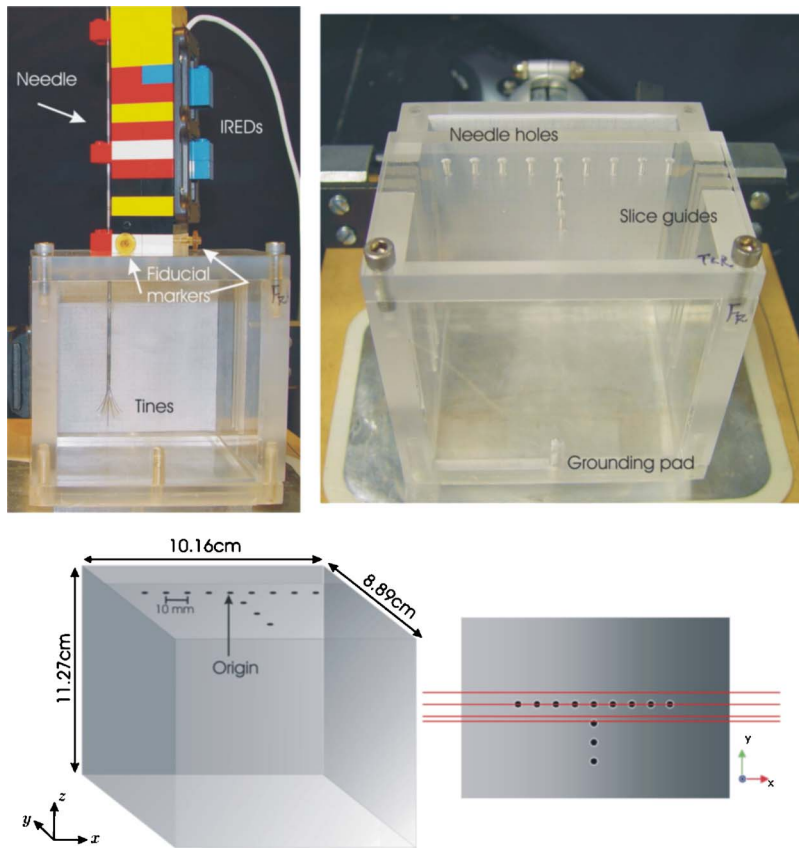
FIG. 4. (top left) Photograph of the phantom housing along with the needle holder and the RFA device in a setup representative of the ablation experiments. (top right) A close-up of the phantom housing showing the needle holes, the slice guides used to aid in cutting the phantom, and the location of the grounding pad. (bottom left) Schematic showing inner dimensions of the phantom housing and its local coordinate systems. The phantom material is filled from the bottom up to an approximate height of 6.5 cm. (bottom right) Top-down view of the phantom housing. The dark circles represent the needle holes. The dark lines show the location of the slice planes. From top to bottom, these planes are y =5, 0, −7, and −9 mm.

proteins, of which albumin is presumably a large component. In making these gels, the agarose solution was prepared initially at a higher concentration and cooled to approximately 50 °C. The egg white solution was warmed to approximately 45 °C, before mixing in the agarose. This step prevented the albumin from being prematurely denatured by the warmer agarose solution, but also allowed the agarose solution to remain above its gelling temperature. The entire solution was then refrigerated for at least 6 h without freezing.

Two ablations were performed, each with constant power settings at 20 W for 10 min using a RITA 500 RF generator and the RITA ablation device. The temperature measurements of the tines were manually recorded at approximately 15 s intervals. The first ablation (designated Case 1 in the remainder of this article) was performed with an initial background temperature, T_0, of 23 °C and an impedance of 26 Ω, as reported by the RITA RF generator. The device was placed through the second needle hold to the left of the center needle hole, as shown in Fig. 4. The second ablation (Case 2) was performed at 27 °C, also with an impedance of 26 Ω. This ablation was performed in the same phantom as in Case 1, but occurred after 1 h of cooling time to allow the phantom material to return to baseline temperatures. The device was placed obliquely into the ablation, as depicted in Fig. 5, to approximately the same depth as the first ablation.

II.B.2. Photogrammetry

After the ablations were performed, the agarose-albumin block was sectioned manually with parallel cuts located at

the planes shown in Fig. 4. These sections were then photographed digitally into images of 1280×960 resolution. The resulting images were rescaled so that the width of the imaged phantom corresponds to the inner diameter of the phantom housing. Finally, the images were realigned so that the edges of the phantom in each image were physically consistent with the shape of the gel system.

II.C. Computational model

A finite element model was developed for the phantom system in order to determine if the ablation results could be predicted by computational modeling. In particular, the model was used to test if the ablation extents align in space with the images of the ablation outcome.

II.C.1. Model geometries

Shown in Fig. 5 is the surface mesh of the domain geometry and the needle model. The model was constructed to mimic the dimensions of the acrylic box. Excluding the RFA device, two material domains were used: One representing the acrylic box and the other the phantom material. The top surface of the model was set so that the total volume would equal 600 mL, consistent with the volume of the phantom material.

The needle geometry of the RFA device in Fig. 5 was constructed to represent the tines deployed at the manufacturer's 2 cm setting. This step was achieved by measuring the average distances of the outer four tine points and the
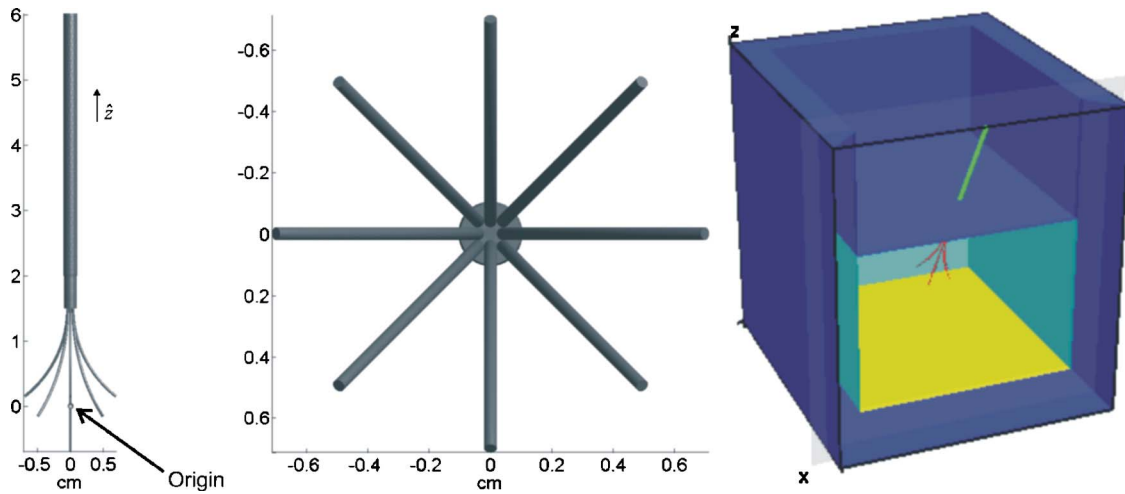
FIG. 5. (left) The surface model of a commercially used ablation device along with its local coordinate system. (middle) A close-up of the tine arrangement from the bottom. The thermocouple readings from the RITA probe correspond to the modeled temperatures at the tips of the outer tines located on the cardinal axes as well as at the tip of the central tine. (right) A cut view of the surface mesh of the phantom geometry with a needle penetrating the phantom surface and placed in the approximate location measured in experimental Case 2.

average distances of the inner four tine points from the axis of the shaft and from the tip of the undeployed device where the tines emerge. For the outer tines, the tips were on average 7.0 mm from the shaft, and 17.9 mm from the undeployed tip; for the inner tines, the distances were 7.0 and 15.2 mm, respectively. The tine tips were then symmetrically arranged around the axis so that the outer and inner tines alternated at 45° intervals, and the outer tine tips corresponding to the location of the thermocouples on the actual RFA device were identified. To create the tines, 0.42 mm diameter tube was extruded along a circular arc connecting the tine tips to the tip of the undeployed device. For the central tine, a straight tube was employed. The needle geometry was then placed according to the orientation and position provided by Optotrak. Achieving this goal required the coregistraton of the needle geometry to the CT image of the physical device. First the shaft of the needle was aligned with the segmented shaft of the CT. Then, the tines of the needle geometry were coregistered with the tine measurements obtained earlier, producing the rigid body transformation $\mathcal{T}_{\text{model}\rightarrow\text{needle}}$. It should be noted that in the last step, the registration was constrained only to rotation about the shaft as well as translation along the shaft. The discrepancy between the nine tines in the coregistered segmented CT needle and in the constructed geometric model was measured as an average distance error. Finally, as in Eq. (2), the total rigid transformation from the local coordinates of the RFA device to the coordinates of the phantom is then given by a series of transformations:

$$\mathcal{T}_{\text{model}\rightarrow\text{phantom}} = \mathcal{T}_{\text{model}\rightarrow\text{needle}} \circ \mathcal{T}_{\text{needle}\rightarrow\text{holder}} \circ \mathcal{T}_{\text{holder}\rightarrow\text{opto}}$$
$$\circ \mathcal{T}_{\text{opto}\rightarrow\text{phantom}}. \tag{3}$$

A mesh was then generated using a freely available meshing software package, Tetgen.[18] Special modifications were made to this software to allow repair of intersecting surfaces

caused, in particular, by the insertion of the needle geometry through the surface of the phantom material.

II.C.2. Constitutive equations

Computational models of thermal ablation start with a thermal diffusion model:

$$\rho c \frac{\partial T}{\partial t} = \nabla \cdot k \nabla T + Q_{\text{RF}}, \tag{4}$$

where Q_{RF} (W/cm^3) is the heat source due to RF currents, and T (°C) is the temperature. All other material coefficients are defined in Table I. The heat source, Q_{RF} can be approximated by first solving the electrostatic problem with appropriate boundary conditions:

TABLE I. List of material properties used in RFA simulation. Values represent the initial properties used in the simulations. As simulations proceed, the temperature-dependent properties change.

Properties	Symbol (units)	Value
Thermal diffusivity (phantom)	k (W/cm·K)	5.72e−3
Density (phantom)	ρ (g/mL)	1.03
Heat capacity (phantom)	c (J/g·K)	3.94
Initial electrical conductivity (phantom)	σ_0 (mS/cm)	4.4
σ Temperature dependence (phantom)	σ_1 (K^{-1})	0.02
Activation energy (phantom)	ΔE_a (J)	3.846e5
Activation factor (phantom)	A (s^{-1})	3.75e57
Thermal diffusivity (acrylic)	k (W/cm·K)	1.7e−3
Density (acrylic)	ρ (g/mL)	1.19
Heat capacity (acrylic)	c (J/g·K)	1.4
Electrical conductivity (acrylic)	σ (mS/cm)	1e−14

$$\nabla \cdot (-\sigma \nabla \Phi) = 0, \tag{5}$$

where $\sigma(S/cm)$ is the conductivity of the medium, and $\Phi(V)$ is the electrostatic potential. Given Φ, the heat source is then estimated as the time-averaged power density generated by the resulting current: $Q_{RF} = (P_{set}/P_0)|\nabla\Phi|^2 \eta/2\sigma$, where P_0 is the input power resulting from 1.0 V being applied to the needle, and P_{set} is the actual power setting, which is 20.0 W. The parameter η represents an empirically determined term to account for the incorrect balance between the source term Q_{RF} and the thermal diffusion parameters in Eq. (4) because of incorrect estimates of properties. In particular as written, η accounts for unknown power losses possibly due to inaccurate parameter selection, discrepancies in the power level reported by the RF generator, or uncertainties in tissue-to-probe coupling. If Eq. (4) is divided through by η, however, it can be interpreted as scaling the thermal properties k and ρc simultaneously to correct for the effects of inaccurate thermal property estimates based on water content. Because the literature values for properties were heavily relied upon in the simulations, errors in both thermal and electrical properties were expected; however, a single corrective factor minimized the need to make measurements of multiple properties. The value of η was set to 90% based on results of a control experiment and used for all subsequent simulations.

The boundary conditions are specified as follows. For the electrostatic problem, the outer surface except the bottom face is prescribed an insulative, no-flux condition. A constant 1.0 V Dirichlet condition is applied on the conductive electrodes, and ground is placed on the bottom face. The total power P_{set} was set to 20 W, and the entire ablation was run for 10 min, after which the power was set to 0 W.

Finally, a measure of accumulated protein denaturation over the course of the ablation is computed. A suitable metric is the Arrhenius damage index, which has been previously employed by investigators to model optical changes in albumin upon heating.[17] It is given by

$$\frac{\partial \omega(\mathbf{x},t)}{\partial t} = -A \exp\left(-\frac{\Delta E_a}{RT(\mathbf{x},t)}\right)\omega(\mathbf{x},t), \tag{6}$$

where R is the universal gas constant, A is the activation factor, and ΔE_a is the activation energy. The prescribed initial condition is $\omega(\mathbf{x},t_0)=1$. The Arrhenius survival function, ω, can be interpreted as the ratio of undenatured proteins to total proteins within a given region of space. Thus in the case of the phantom, $\omega=1$ corresponds to albumin in its native state, whereas $\omega=0$ indicates that the albumin is completely denatured. In this work, the threshold used to demarcate the denatured coagulum was set to $\omega_0=e^{-1}$ or approximately 37%.

II.C.3. Material properties

As suggested previously by other investigators,[12,19] this model implemented temperature dependent electrical conductivity. In particular, the electrical conductivity of ionic solutions, notably that of the phantom material, increases at a rate of 2%/°C.[20,21] Thus, the conductivity of the phantom is

given as $\sigma=\sigma_0(1+\sigma_1(T-T_0))$, where the coefficients σ_0 and σ_1 are given in Table I above, and T_0 is the baseline temperature. The temperature dependence of other parameters was not modeled because their inclusion in the model would produce relatively small changes in the final temperature.[22] As the mesh was regenerated for each needle placement, routines are implemented to assign appropriate material properties to each tetrahedral element.

A method for estimating the thermal properties was proposed in Ref. 17 based on the estimated water content of the material by mass and adopted in this study. The water content of the phantom was estimated based on the protein content (albumin) and agarose (56 g) as compared to the total mass of the gel (600 g), resulting in a ratio of 93%. The electrical conductivity of the phantom was estimated to be 4.4 mS/cm at 23 °C based upon the impedance reported by the generator, and using the assumption that the material was homogeneous. Finally, the Arrhenius parameters were those used in Ref. 17.

II.C.4. Iterative solver

In order to solve the coupled equations, the finite element method (FEM)[11,12,23,24] was used to discretize the problem spatially. An iterative solver package (PETSc[25]) was used to obtain the solution of the resulting systems of equations using an iterative scheme. The transient temperature solution was computed over 15 min via a fully implicit time-stepping scheme, at intervals of 15 s. Temperature-dependent properties were updated by using the temperature distribution from the previous iteration. A constant power setting was imposed on the electrostatic problem by scaling the total power in the domain to 20.0 W at every time step. After 10 min of ablation, the applied power was set to zero. All algorithms were implemented in C++ on a Win32 platform using a Pentium 3.4 GHz processor with 2 GB of RAM. Further details on the implementation can be found in Ref. 26.

II.C.5. Image comparison with model results

In order to evaluate the accuracy of the model two parameters were developed based on the pixels from the imaging studies of the phantom results. The sensitivity, S, measures the ratio of the number of ablated pixels, which coincide with the model, $N_{overlap}$, to the total number of segmented pixels, $N_{observed}$: $S=N_{overlap}/N_{observed}$. The positive predictive value, P, measures the ratio of the overlap of ablated pixels with the model to the total number of pixels inside the model, $N_{predicted}$: $P=N_{overlap}/N_{predicted}$. As an illustration, a large sphere that covers the entire region of interest would result in a S value of 1, but at the cost of a low P. At the other extreme, a model that predicts a tiny spherical ablation in the middle of the observed ablation pixels would have a high P but a low S. It is desirable to have high S and P values because it implies the model would be able to predict the observed ablation results with high probability without the model's being overly permissive in predicting ablated pixels.
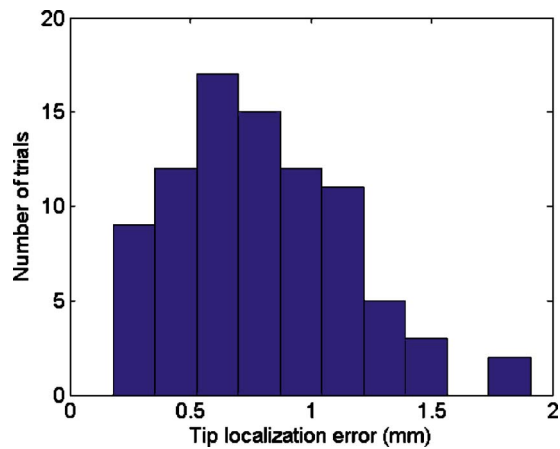
FIG. 6. Histogram of the distance between needle tip location predicted by Optotrak and as observed in CT imaging.

In anticipation of needle tracking inaccuracies, a method was created to test whether the model accuracy, as quantified by the parameters given above, would improve only by changing the position of the needle, while the other model parameters remained the same. Intuitively, the RFA needle position that produces ablation extents maximally registered with the imaged ablation would provide an estimate of the true location of the device, and the difference in positions would thus give an estimate of the tracking inaccuracy. The details of the maximization scheme can be found in Ref. 26. Briefly, the RFA needle was repositioned from the measured placement with the objective of overlapping more of the imaged pixels classified as ablated with the model prediction of the ablation zone. For each new placement of the needle, the mesh of the phantom was recreated with the updated position of the RFA surface geometry, and a new model solution was computed. By coupling the model and mesh generation with a numerical optimization scheme, successive RFA needle placements could be automatically tested until the overlap between imaged and modeled ablations was maximized. In order to reduce the need to solve a model for each new test placement, the optimization scheme employed a heuristic in which the ablation extents were assumed to move rigidly with the RFA needle. After several steps of optimization, the ablation extents were updated with a model solution using the most recent test placement of the RFA needle. The metrics S and P were then reevaluated for the optimized needle position. Finally, these metrics were also computed for models based on spherical geometries, which are commonly used in the ablation literature to simulate ablations.

III. RESULTS

III.A. Needle tracking experiments

The average needle placement error, $\bar{\delta}$, over all trials was 1.4 ± 0.6 mm, and Fig. 6 shows the calculated localization error distributions. This result is comparable to a previous study using a similar barium track technique for evaluating needle tip tracking in gene therapy application.[27] One source

of uncertainty in this experiment is the distribution of barium within the needle track. Because gelatin tends to crack upon applied stress, the barium tracks may have extended laterally from the tines in an asymmetric manner. This source of error may be constrained in the future by reducing the total volume of barium injected.

III.B. Phantom experiments

III.B.1. Tine coregistration

The registration error in $\mathcal{T}_{\text{model} \rightarrow \text{needle}}$ used to map the tine tips of the needle geometry used in FEM modeling to those of the physical needle was 0.88 mm. This result reflects discrepancies between the symmetric arrangement of the tines used in modeling compared with the actual asymmetries in the physical device. Ideally, the geometry should match that of the physical device since electrical power is concentrated in the tine tips, and, thus, accurate localization of the tine tips could potentially produce more accurate modeling. Nevertheless this result is reasonable given the inherent difficulty in localizing flexible mechanical systems such as the tines in the RFA device.

III.B.2. Temperature traces

The RITA RF system contains thermocouples embedded in the outer tines, and, during the ablation experiments, these measurements were recorded manually. The tines have been labeled to match the scheme used by RITA, in which tine 1 is the center tine, and tines 2 through 5 are the outermost tines, corresponding to the tines placed on the cardinal axes shown in Fig. 5. As graphed in Fig. 7, the temperature measurements agreed with the model predictions well. At higher temperatures, however, there is some deviation with the model, particularly visible in the plot for Case 1. This discrepancy is likely the result of additional dynamics, such as vaporization of water, or the desiccation of the phantom resulting in decreased power delivery locally. The FEM model does not currently include these dynamics. In both placements, tine 1 is closest to ground, and hence experiences the least resistance for the RF current. Thus, more power is preferentially deposited there. Also of note is that even though the remaining 4 tines are arranged symmetrically about the axis of the device, there is some difference between the temperature distributions. This difference is most noticeable in Case 2, in which the tines are placed at different distances from ground because of the oblique angle of insertion. The most straightforward explanation of these differences in local temperature is that they are the results of boundary effects.

III.B.3. Image analysis

The imaged ablation outcomes were segmented using a thresholding scheme. The processed image corresponding to the slice plane $y = 0$ mm, as displayed in Fig. 8, is updated in Fig. 9. The measured needle placements were generally in the right vicinity of the corresponding ablation for each case.
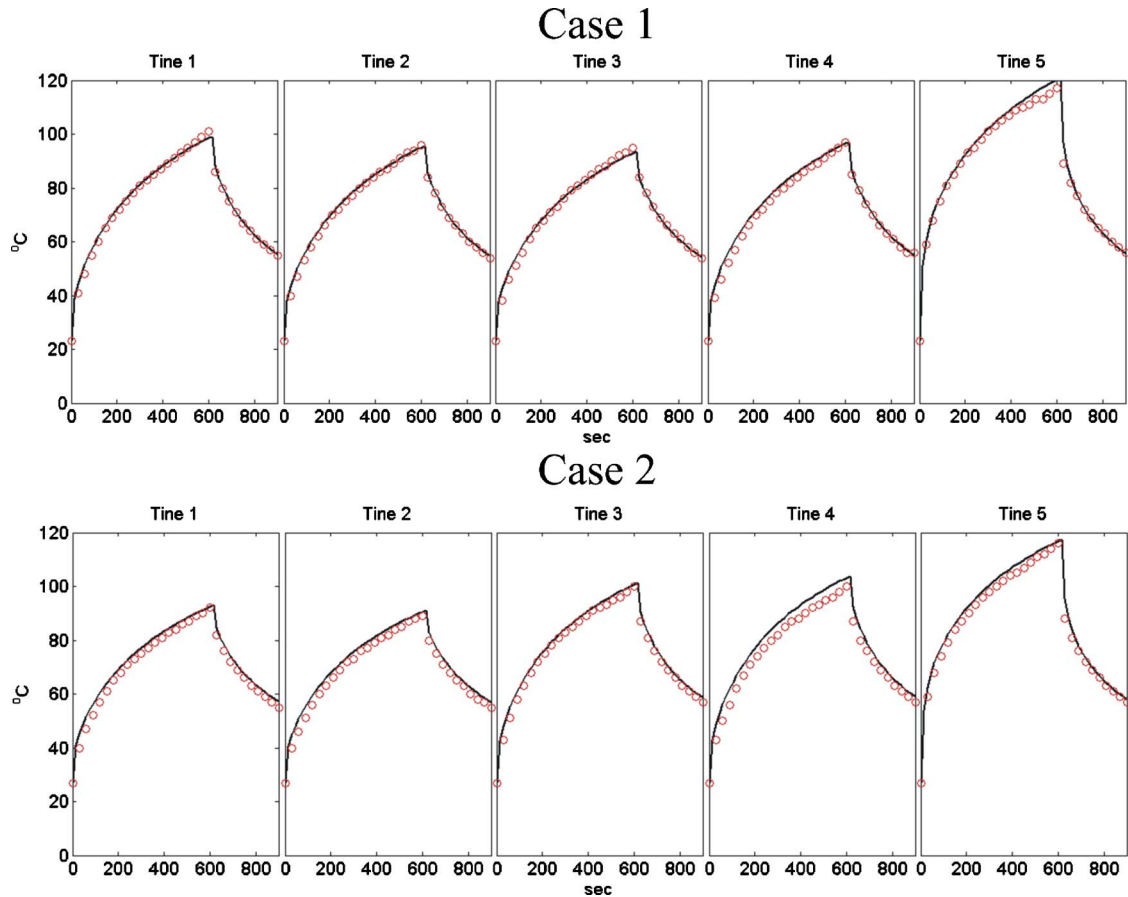
FIG. 7. Temperature traces from (left) Case 1 and (right) Case 2. The marked points are the recorded temperatures provided by the RFA system. The solid lines represent the model predictions.

Furthermore, the modeled ablations agreed with the imaged ablations. The next sections provide a quantification of this agreement.

III.B.4. Model accuracy

The results presented in the table demonstrate that with the raw measurements of needle position, the model is capable of predicting at least 90% of the pixels that had been classified as being ablated. In achieving this result, however,

the model predicted roughly 17%–19% more pixels (i.e., from calculating the ratio of S to P) as ablated than were classified as being ablated. The overestimation of the ablation extents is likely a result of inaccurate model parameters. On the other hand, the differences in S values between the two cases may be perhaps better explained by inaccurate needle tracking.

III.B.5. Needle repositioning

Table II lists the results from repositioning the needle in model simulations in an attempt to increase the model over-

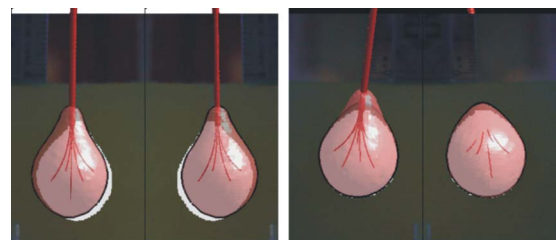FIG. 8. Ablation outcome for the slice at $y=0$ mm.

FIG. 9. Ablations at slice $y=0$ mm for (left pair) Case 1 and (right pair) Case 2. In each pair, the left image depicts the camera view and the right image the back view. The light mask represents the segmented pixels corresponding to the ablated albumin. The surfaces provide a 3D context of the overall ablation shapes. The intersection of the surface with the plane is given by the black outline.

TABLE II. Table of parameters characterizing model accuracy. The bottom row lists the maximum displacement of a tine in the repositioning process.

	Case 1		Case 2	
	Original	Repositioned	Original	Repositioned
S_{FEM}	91.6%	99.1%	99.4%	99.9%
P_{FEM}	77.9%	82.6%	83.7%	81.8%
S_{sphere}	—	81.5%	—	71.3%
P_{sphere}	—	100%	—	100%
Max tine shift	1.4 mm		1.7 mm	

lap with observed pixels. In both cases, the S values increased, an expected result since the goal was to increase the numerator of S. In particular, with Case 1, the data suggest that the needle tracking error was a major contributor to the reported inaccuracies as both S and P increased while the ratio of S to P slightly increased from 18% to 19%, suggesting that the modeled ablation could capture more pixels simply by reposition rather than by increasing its size. In Case 2, however, there was a marginal increase in S while P decreased. This result indicated that the algorithm positioned the needle in a manner that produced a larger ablation in order to overlap more ablated pixels. Nevertheless the decrease in P was marginal, and the fact that both cases had roughly the same value of P suggests that some shared parameters used in modeling the ablations were likely affecting the overestimation of the ablation size. These parameters may include discrepancies between true and simulated material properties, or the incorrect choice of threshold, ω_0. This latter prospect is further explored below. It is of note that if the repositioned needle represents the true location of the physical device, then the amount of displacement of the tines is comparable to the error reported in the needle tracking experiment above.

III.B.6. Comparison with sphere fits

The results obtained with the repositioned FEM models were compared with spherical ablation geometries. Each of the corrected ablation zones was fit with the largest sphere that was entirely contained within the observed pixels. The

results shown in Fig. 10 demonstrate that a sphere model fits the fatter portion of the teardrop-shaped ablation, but fails to account for the narrower portion near the shaft of the device. This observation is further illustrated in Fig. 11, in which the model accuracy was quantified using the S and P values described earlier. For the repositioned FEM model, these curves were created by varying the threshold Arrhenius survival fraction. For the sphere model, they were generated by varying the radius of the fitted spheres. In general, in order to achieve an S value that is greater than 90%, the graphs show that the FEM model were able to do so at a higher P than using the sphere model. In other words, if both model were fitted to capture 90% of the observed ablated pixels, the sphere fitted model would contain more nonablated pixels than the FEM model. Although these results may seem to favor FEM only slightly, it is worth mentioning that these phantoms do not include the effects of vasculature. In those circumstances, the FEM model may outperform spherical models more appreciably because geometric models do not account for heat sink effects. In addition, there is little doubt that in the case of large tumors where multiple ablations may be necessary, it is likely that FEM models will be better at predicting the combined effects of nearby ablation sites. It remains to be seen if the methods proposed in Ref. 10, will enhance the predictivity of the geometric models.

IV. DISCUSSION

Successful treatment with RFA requires a predictive model of therapeutic outcome given a particular placement
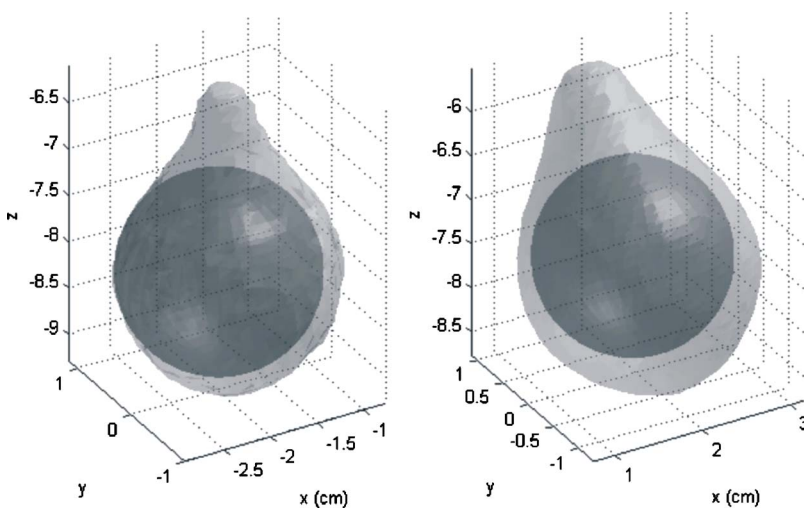

FIG. 10. The diagram shows, in the coordinate system of the phantom, the largest spheres that fit the ablated pixels with the corresponding FEM prediction overlaid. (left) Case 1. (right) Case 2.
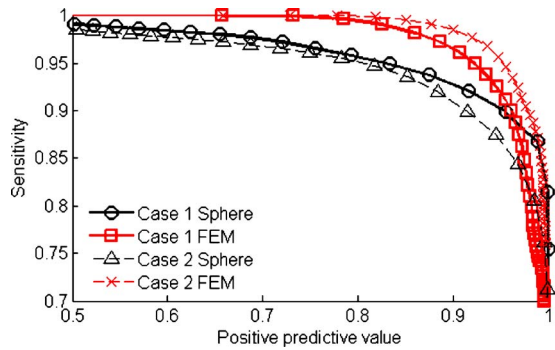
FIG. 11. Receiver operator characteristics of sensitivity, S, and positive predictive value, P, values using sphere and FEM ablation models for each of the two ablation results. The curve was generated for the FEM model by varying the contour threshold, whereas for the sphere model, the sphere radius was varied.

of the RFA needle as well as a means of implementing the planned placement to within tolerable accuracy.[6] Despite various schemes described in the literature to develop a treatment plan and execute it via guided RFA, we are not aware of any effort to evaluate the systems by comparing the planned and actual ablation zones. Because targeting inaccuracy results in a decreased overlap between the ablation zone and the intended treatment volume, current treatment strategies attempt to enlarge the ablation volume either by employing multiple ablations[28] or by modifying device characteristics and performance to deliver more power.[29] Nevertheless, these strategies are not sufficient toward creating robust plans. The use of multiple ablations has been previously explored by modeling ablations as spheres or ellipsoids; however, these geometrics models are not sensitive to the actual physical parameters that affect ablation volume. Employing more powerful ablation systems does not obviate the need for careful placement planning with accurate models. Using guidance to implement plans created with predictive, physical models is ultimately necessary to deliver treatments that are robust to the effects of guidance error, that minimize the rate of incomplete treatment, and that reduce the total treatment time. Our work represents a first step toward this goal by simultaneously characterizing the accuracy of an optically tracked RFA device as well as the resulting discrepancies between the predicted and imaged ablation outcomes in single ablations.

It has been suggested that targeting to within 5 mm accuracy is sufficient for current surgical needs.[30] The tracking accuracy presented in the results fall within the reported 5 mm limit, but the experimental setup in this work does not reflect other surgical conditions in which problems of organ deformation along with larger registration errors are present. While methods to deal with these issues are actively being explored, including investigations into model-updated guidance schemes,[31] the methods presented above are not dependent on the actual guidance technique. Indeed, for any guidance technology adapted to RFA applications, there will remain a need to characterize its targeting accuracy in phantom. This work presented two independent methods of evaluating the targeting that produced consistent results showing approximately 2 mm of targeting error. The roughly 90% overlap between the imaged ablation and the model predicted ablation suggests that physical models can indeed be adapted to plan and guide ablations. Although our results are encouraging, a more direct method to evaluate the planned ablation is desirable, such as an imaging system that shows both the ablation outcome and the location of the RFA needle simultaneously. Nevertheless, we are not presently aware of any imaging modality that does both without incurring imaging artifacts, especially due to the presence of a metallic object. This problem is currently being pursued.

The reported discrepancy between imaged and predicted ablations is likely the result of multiple sources of errors, primarily from the uncertainties in the physical properties of the phantom, inaccuracies in the geometric model of the RFA device used for FEM modeling, and tracking inaccuracies of the needle in a nonrigid medium. Decoupling the contributions of each of these uncertainties will require further work. We attempted to control for these uncertainties by calibrating with an empirical correction factor, η, to the RF power term. Using this calibration scheme, our model results produced discrepancies between predicted and temperatures measurements that were comparable to those previously reported in the ablation literature.[32] This result, coupled with the closely matching shapes of the model predictions and the imaged ablations, provides evidence that the model may be adequate for planning.

V. CONCLUSIONS

In this article, evidence was presented to support the use of a tracked RFA device in producing ablations whose spatial extents are consistent with results from computational modeling. Needle placement experiments demonstrated the ability of the optical tracking system to localize functional features of the device, particularly the electrodes, in space. The ablations were performed inside a phantom system with the tracked device, and the positional data of the device were used in computational models of the ablation to generate predictive models of ablation extents. The results from the simulations demonstrated the capability of the models to predict at least 90% of the ablated pixels in images of the phantom. In addition, while recent investigations using partial differential equations to correct for organ deformations during image-guided surgery have begun to be realized, this is the first article to demonstrate a similar model-updating methodology within a completely new constitutive framework.

ACKNOWLEDGMENTS

a)Author to whom correspondence should be addressed. Electronic mail: richard.chen@vanderbilt.edu

[1]K. K. Ng and R. T. Poon, "Radiofrequency ablation for malignant liver tumor," Surg. Oncol. **14**, 41–52 (2005).

[2]D. Haemmerich, T. Staelin, S. Tungjitkusolmun, F. T. Lee, Jr., D. M. Mahvi, and J. G. Webster, "Hepatic bipolar radio-frequency ablation between separated multiprong electrodes," IEEE Trans. Biomed. Eng. **48**, 1145–1152 (2001).

[3]H. Rhim, S. N. Goldberg, G. D. Dodd, 3rd, L. Solbiati, H. K. Lim, M. Tonolini, and O. K. Cho, "Essential techniques for successful radiofrequency thermal ablation of malignant hepatic tumors," Radiographics **21** S17–35;discussion S36–39 (2001).

[4]D. J. Scott, W. N. Young, L. M. Watumull, G. Lindberg, J. B. Fleming, J. F. Huth, R. V. Rege, D. R. Jeyarajah, and D. B. Jones, "Accuracy and effectiveness of laparoscopic vs open hepatic radiofrequency ablation," Surg. Endosc **15**, 135–140 (2001).

[5]S. C. Rose, T. I. Hassanein, D. W. Easter, R. A. Gamagami, M. Bouvet, D. H. Pretorius, T. R. Nelson, T. B. Kinney, and G. M. James, "Value of three-dimensional US for optimizing guidance for ablating focal liver tumors," J. Vasc. Interv. Radiol. **12**, 507–515 (2001).

[6]F. Banovac, J. Tang, S. Xu, D. Lindisch, H. Y. Chung, E. B. Levy, T. Chang, M. F. McCullough, Z. Yaniv, B. J. Wood, and K. Cleary, "Precision targeting of liver lesions using a novel electromagnetic navigation device in physiologic phantom and swine," Med. Phys. **32**, 2698–2705 (2005).

[7]G. Antoch, H. Kuehl, F. M. Vogt, J. F. Debatin, and J. Stattaus, "Value of CT volume imaging for optimal placement of radiofrequency ablation probes in liver lesions," J. Vasc. Interv. Radiol. **13**, 1155–1161 (2002).

[8]E. Sjolie, T. Lango, B. Ystgaard, G. A. Tangen, T. A. N. Hernes, and R. Marvik, "3D ultrasound-based navigation for radiofrequency thermal ablation in the treatment of liver malignancies," Surg. Endosc **17**, 933–938 (2003).

[9]G. D. Dodd, 3rd, M. S. Frank, M. Aribandi, S. Chopra, and K. N. Chintapalli, "Radiofrequency thermal ablation: computer analysis of the size of the thermal injury created by overlapping ablations," AJR, Am. J. Roentgenol. **177**, 777–782 (2001).

[10]C. Villard, L. Soler, and A. Gangi, "Radiofrequency ablation of hepatic tumors: simulation, planning, and contribution of virtual reality and haptics," Comput. Methods Biomech. Biomed. Eng. **8**, 215–227 (2005).

[11]S. Tungjitkusolmun, S. T. Staelin, D. Haemmerich, J. Z. Tsai, H. Cao, J. G. Webster, F. T. Lee, D. M. Mahvi, and V. R. Vorperian, "Three-dimensional finite-element analyses for radio-frequency hepatic tumor ablation," IEEE Trans. Biomed. Eng. **49**, 3–9 (2002).

[12]I. A. Chang and U. D. Nguyen, "Thermal modeling of lesion growth with radiofrequency ablation devices," Biomed. Eng. Online **3**, 27 (2004).

[13]R. Baissalov, G. A. Sandison, D. Reynolds, and K. Muldrew, "Simultaneous optimization of cryoprobe placement and thermal protocol for cryosurgery," Phys. Med. Biol. **46**, 1799–1814 (2001).

[14]D. C. Lung, T. F. Stahovich, and Y. Rabin, "Computerized planning for multiprobe cryosurgery using a force-field analogy," Comput. Methods Biomech. Biomed. Eng. **7**, 101–110 (2004).

[15]T. W. Sheu, C. W. Chou, S. F. Tsai, and P. C. Liang, "Three-dimensional analysis for radio-frequency ablation of liver tumor with blood perfusion effect," Comput. Methods Biomech. Biomed. Eng. **8**, 229–240 (2005).

[16]C. R. Maurer, Jr., J. M. Fitzpatrick, M. Y. Wang, R. L. Galloway, Jr., R. J. Maciunas, and G. S. Allen, "Registration of head volume images using implantable fiducial markers," IEEE Trans. Med. Imaging **16**, 447–462 (1997).

[17]M. N. Iizuka, M. D. Sherar, and I. A. Vitkin, "Optical phantom materials for near infrared laser photocoagulation studies," Lasers Surg. Med. **25**, 159–169 (1999).

[18]H. Si, "Tetgen," 1.3.4 ed. (Berlin, 2005).

[19]L. J. Hayes, K. R. Diller, J. A. Pearce, M. R. Schick, and D. P. Colvin, "Prediction of transient temperature fields and cumulative tissue destruction for radio frequency heating of a tumor," Med. Phys. **12**, 684–692 (1985).

[20]K. R. Foster and H. P. Schwan, "Dielectric properties of tissues and biological materials: a critical review," Crit. Rev. Biomed. Eng. **17**, 25–104 (1989).

[21]M. Pop, A. Molckovsky, L. Chin, M. C. Kolios, M. A. Jewett, and M. D. Sherar, "Changes in dielectric properties at 460 kHz of kidney and fat during heating: importance for radio-frequency thermal therapy," Phys. Med. Biol. **48**, 2509–2525 (2003).

[22]A. V. Shahidi and P. Savard, "A finite element model for radiofrequency ablation of the myocardium," IEEE Trans. Biomed. Eng. **41**, 963–968 (1994).

[23]D. Haemmerich, S. Tungjitkusolmun, S. T. Staelin, F. T. Lee, D. M. Mahvi, and J. G. Webster, "Finite-element analysis of hepatic multiple probe radio-frequency ablation," IEEE Trans. Biomed. Eng. **49**, 836–842 (2002).

[24]T. P. Ryan and S. H. Goldberg, "Comparison of simulation and experimental results for RF thermal treatment devices with or without cooling," presented at Proceedings of Thermal Treatment of Tissue with Image Guidance, San Jose, CA, 1999.

[25]S. Balay, K. Buschelman, W. D. Gropp, D. Kaushik, M. G. Knepley, L. C. McInnes, B. F. Smith, and H. Zhang, "PETSc," 2.3.0 ed., 2005.

[26]C.-C. R. Chen, "Planning needle placement in image-guided radiofrequency ablation of hepatic tumors," in *Biomedical Engineering* (Vanderbilt University, Nashville, 2006), Ph.D. thesis dissertation, Department of Biomedical Engineering.

[27]S. S. Harris, D. Hallahan, and J. Robert, L. Galloway, "A technique for validating image-guided gene therapy," presented at Medical Imaging 2003: Visualization, Image-Guided Procedures, and Display, 2003.

[28]M. H. Chen, W. Yang, K. Yan, M. W. Zou, L. Solbiati, J. B. Liu, and Y. Dai, "Large liver tumors: protocol for radiofrequency ablation and its clinical application in 110 patients—mathematic model, overlapping mode, and electrode placement process," Radiology **232**, 260–271 (2004).

[29]S. Mulier, Y. Ni, Y. Miao, A. Rosiere, A. Khoury, G. Marchal, and L. Michel, "Size and geometry of hepatic radiofrequency lesions," Eur. J. Surg. Oncol. **29**, 867–878 (2003).

[30]S. Nicolau, A. Garcia, X. Pennec, L. Soler, and N. Ayache, "An augmented reality system to guide radio-frequency tumour ablation," in *Computer Animation and Virtual Worlds* (2005), Vol. 16, pp. 1–10.

[31]D. M. Cash, M. I. Miga, T. K. Sinha, R. L. Galloway, and W. C. Chapman, "Compensating for intraoperative soft-tissue deformations using incomplete surface data and finite elements," IEEE Trans. Med. Imaging **24**, 1479–1491 (2005).

[32]M. N. Iizuka, I. A. Vitkin, M. C. Kolios, and M. D. Sherar, "The effects of dynamic optical properties during interstitial laser photocoagulation," Phys. Med. Biol. **45**, 1335–1357 (2000).